NANO LETTERS

Letter

pubs.acs.org/NanoLett

Gate-Tunable Conducting Oxide Metasurfaces

Yao-Wei Huang,[†,‡,§] Ho Wai Howard Lee,[†,‡] Ruzan Sokhoyan,[†] Ragip A. Pala,[†,‡] Krishnan Thyagarajan,[†,‡] Seunghoon Han,[†,∥] Din Ping Tsai,[§,⊥] and Harry A. Atwater*[,†,‡]

[†]Thomas J. Watson Laboratories of Applied Physics and [‡]Kavli Nanoscience Institute, California Institute of Technology, Pasadena, California 91125, United States

[§]Department of Physics, National Taiwan University, Taipei 10617, Taiwan

[∥]Samsung Advanced Institute of Technology, Samsung Electronics, Suwon-si, Gyeonggi-do 443-803, Republic of Korea

[⊥]Research Center for Applied Sciences, Academia Sinica, Taipei 11529, Taiwan

S *Supporting Information*

ABSTRACT: Metasurfaces composed of planar arrays of subwavelength artificial structures show promise for extraordinary light manipulation. They have yielded novel ultrathin optical components such as flat lenses, wave plates, holographic surfaces, and orbital angular momentum manipulation and detection over a broad range of the electromagnetic spectrum. However, the optical properties of metasurfaces developed to date do not allow for versatile tunability of reflected or transmitted wave amplitude and phase after their fabrication, thus limiting their use in a wide range of applications. Here, we experimentally demonstrate a gate-tunable metasurface that enables dynamic electrical control of the phase and amplitude of the plane wave reflected from the metasurface. Tunability arises from field-effect modulation of the complex refractive index of conducting oxide layers incorporated into metasurface antenna elements which are configured in reflectarray geometry. We measure a phase shift of 180° and ~30% change in the reflectance by applying 2.5 V gate bias. Additionally, we demonstrate modulation at frequencies exceeding 10 MHz and electrical switching of ±1 order diffracted beams by electrical control over subgroups of metasurface elements, a basic requirement for electrically tunable beam-steering phased array metasurfaces. In principle, electrically gated phase and amplitude control allows for electrical addressability of individual metasurface elements and opens the path to applications in ultrathin optical components for imaging and sensing technologies, such as reconfigurable beam steering devices, dynamic holograms, tunable ultrathin lenses, nanoprojectors, and nanoscale spatial light modulators.

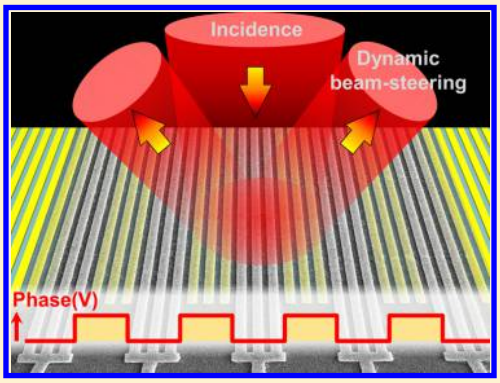

KEYWORDS: *Metasurfaces, transparent conducting oxides, field-effect modulation, phase modulation, epsilon-near-zero materials, plasmonics, modulators, beam steering*

Metasurfaces are arrays of subwavelength elements, in which, each element is configured to control the phase and amplitude of the transmitted, reflected, and scattered light.[1−3] By controlling the phase shift and amplitude change imposed by each metasurface element, we can realize phased arrays that would enable complex wavefront engineering. Significant advances in subwavelength-scale fabrication and theoretical modeling tools in the past decade, enabled the development of a generalized form of Snell's law with ordinary and anomalous refraction, metasurfaces that refract and focus light, opening up new pathways to realize holograms,[4−7] optical vortex generation/detection, ultrathin focusing lens, photonic spin Hall effect,[8−11] among others. Metasurfaces can also control beam polarization, yielding linearly, elliptically, circularly or radially polarized light.[4,12] Because of the flat nature of metasurfaces (typical thickness <100 nm), conventional three-dimensional optical elements such as prisms or lenses can be replaced by their flat, low-profile analogs. An important practical consequence of the flat geometry is that metasurfaces are easy to fabricate via planar lithographic processing.

Passive metasurfaces have been demonstrated in the spectral region ranging from the visible to microwave frequencies. An as-yet unrealized milestone in the field is to achieve an actively tunable metasurface with arbitrary control of phase and amplitude of individual antenna elements by postfabrication electrical modulation. This would enable dynamical wavefront control in thin flat optical devices, such as dynamical beam steering, reconfigurable imaging, tunable ultrathin lens, and high capacity data storage. Previously, active control of overall metasurface amplitude response has been reported, using various physical mechanisms.[13−23] However, to realize the full potential offered by dynamic tunability control of the phase of

Received: February 7, 2016
Revised: August 6, 2016
Published: August 26, 2016

DOI: 10.1021/acs.nanolett.6b00555
Nano Lett. 2016, 16, 5319−5325

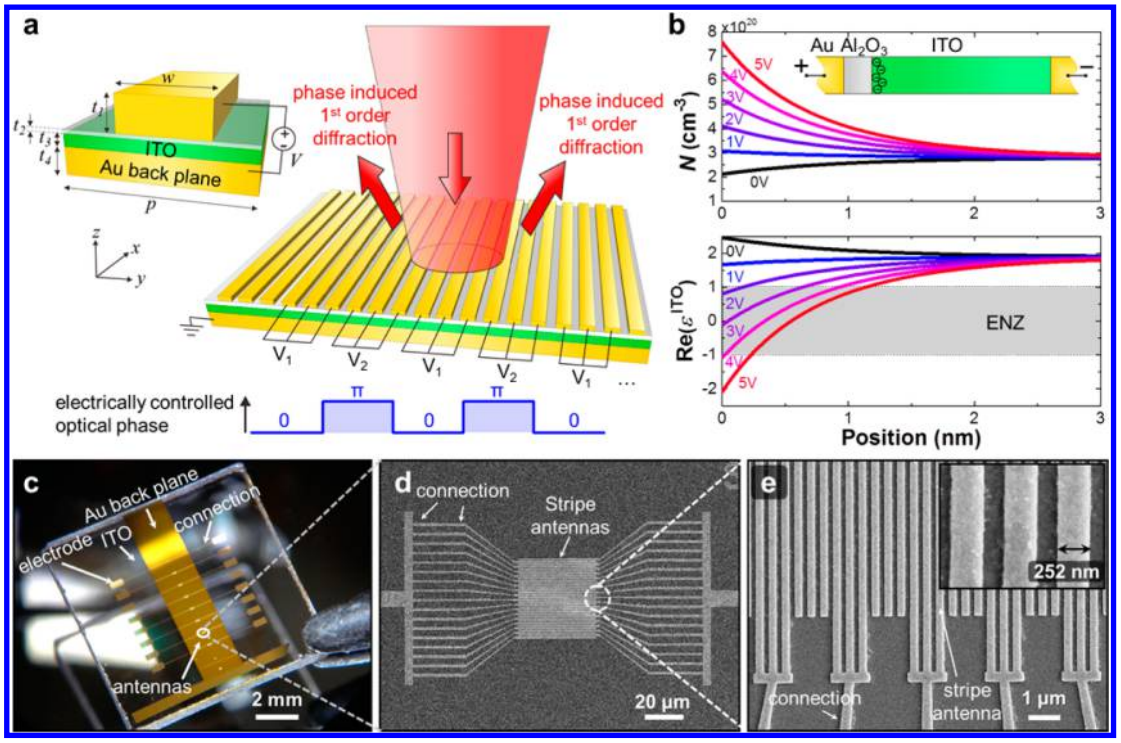

Figure 1. Gate-tunable metasurface. (a) Schematic of the tunable metasurface. The structure consists of a quartz substrate, gold back plane, and a thin ITO film followed by a thin alumina film on which we pattern connected gold stripe nanoantenna array. Voltage is applied between the stripe antenna and the bottom gold resulting in the formation of charge accumulation at the Al_2O_3/ITO interface. Unit cell dimensions are chosen as follows: width of stripe antenna w = 250 nm, thicknesses of the stripe antenna, Al_2O_3, ITO, and Au back plane are t_1 = 50 nm, t_2 = 5 nm, t_3 = 20 nm, t_4 = 80 nm, respectively. The periodicity of the unit cell is p = 400 nm. (b) Operation principle of the tunable metasurface is based on MOS field-effect dynamics. When applied voltage is sufficiently high, an electron accumulation region forms in ITO at the Al_2O_3/ITO interface (inset). (Top panel) Spatial distribution of the carrier concentration N for different applied voltages. (Bottom panel) Real part of the dielectric permittivity of ITO ε_r^{ITO} at wavelength of 1500 nm as a function of distance from Al_2O_3/ITO interface for different applied voltages. Gray area highlights the spatial region where ε_r^{ITO} acquires values between 1 and −1 representing the ENZ region. (c) Photographic image of the fabricated structure. For gate biasing, stripe antennas are connected to electrodes. (d,e) Scanning electron microscopy images of (d) the stripe antenna and connections and (e) the close-up of stripe antenna.

individual metasurface elements is required. To date, there has been no comprehensive experimental validation of the promise for dynamical control of both the wave phase and the amplitude, either in reflection or transmission at optical frequencies from individual phase elements that comprise a metasurface. Here, we experimentally demonstrate independent electrical addressability of metasurface elements. This enables electrical switching of ±1 order diffracted beams. Such an electrically gate-tunable structure allows for addressing individual metasurface elements and completes integration with electronics.

Among various physical mechanisms for modulation of complex refractive index, field-effect modulation is a distinctly attractive approach because of the combined advantages of high speed modulation of large numbers of individual metasurface elements and extremely low power dissipation. Field-effect modulation is ubiquitous in semiconductor electronics and is the principle underlying contemporary low power-integrated circuit performance. On the basis of the formation of charge depletion or accumulation regions in doped semiconductors (e.g., metal-oxide−semiconductor field-effect transistors and thin-film transistors), field effect modulation can provide a sufficiently large carrier density change in a heavily doped semiconductor or conducting oxide, which results in a large variation of its complex refractive index in the charge accumulation or depletion regions.[24,25] This phenomenon has been used to demonstrate electrically controlled plasmonic amplitude modulators in a metal-oxide−semiconductor (MOS) configuration, where coupling of modulator output power into a waveguide is controlled by an electrical bias across the metal−semiconductor field effect channel.[24−26] Transparent conducting oxide (TCO) materials,[27,28] such as indium tin oxide (ITO), have also been used as the active semiconductor layer.[24,26,29−32] The results reported in these studies suggest that applying an electrical bias between metal and ITO changes the sign of ε_r^{ITO}, the real part of the dielectric permittivity of ITO in the accumulation layer from positive to negative. When $|\varepsilon_r^{ITO}|$ is in the epsilon-near-zero (ENZ) region, that is, $-1 < \varepsilon_r^{ITO} < 1$, a large electric field enhancement occurs in the accumulation layer for near-infrared wavelengths,[21,26,33,34] providing an efficient way to electrically modulate the optical properties of nanophotonic devices with high modulation speed and low power consumption.

Here we integrate field-effect tunable materials with metasurfaces to demonstrate a dynamically tunable metasurface that for the first time allows active control of both reflected light phase and amplitude at near-infrared wavelengths. The metasurface (patch antenna geometry) we study consists of a gold back plane, an ITO layer followed by an aluminum oxide layer on which we pattern a gold stripe antenna array (Figure 1a). The identical antennas are connected either to right or left external gold electrodes to create electrical gates. Unlike

DOI: 10.1021/acs.nanolett.6b00555
Nano Lett. 2016, 16, 5319−5325

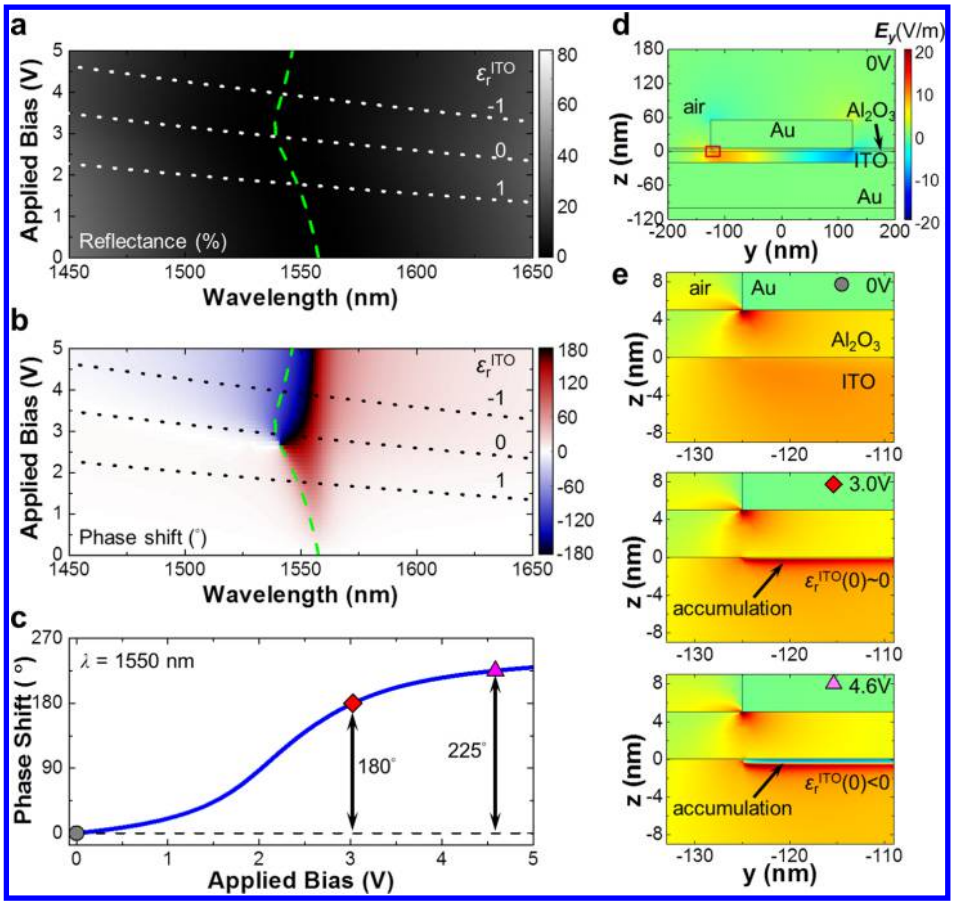

Figure 2. Gate-tunable metasurface based on interplay between magnetic plasmon resonance and ENZ region in ITO. Simulated (a) reflectance and (b) phase shift due to gating as a function of wavelength and applied voltage. The phase shift is plotted with respect to the reflected phase from the metasurface without applied voltage. The dotted lines show points in $V-\lambda$ parameter space for which permittivity of ITO equals from −1, 0, or 1 at the Al_2O_3/ITO interface, representing the ENZ region in the accumulation layer. The green dashed line marks the position of a reflectance dip corresponding to the magnetic dipole resonance. (c) Simulated phase shift as a function of applied bias at wavelength of 1550 nm. (d) Spatial distribution of the z component of the electric field E_z, and (e) the magnified region near the Al_2O_3/ITO interface for applied bias of 0, 3.0, and 4.6 V at wavelength of λ = 1550 nm.

previous optical frequency metasurfaces that utilized variations in the antenna geometry or orientation to impose different phase shifts for each antenna element, the metasurface we study here is periodic and a dynamic control over the phase shift at each metasurface element is achieved by applying bias voltages to combinations of adjacent antenna electrodes. Each metasurface antenna element is effectively an MOS capacitor with the Au antenna serving as a gate and ITO functioning as a field effect channel (inset of Figure 1a). When applying an electrical bias between the antenna gate and the underlying ground plane, the carrier concentration at the Al_2O_3/ITO interface increases or decreases by forming a charge accumulation or depletion layer, respectively. This results in modulation of the complex permittivity of ITO, which alters the interaction of the incident light with the antenna and modulates the reflection from the surface. The variation of the reflected phase and amplitude at each antenna element is amplified when the real part of the dielectric permittivity in the ITO accumulation layer changes its sign from positive to negative (Figure 1b).

To obtain the physical parameters for the ITO layers incorporated in our devices, we fabricated additional ITO-on-glass samples for Hall measurements and ITO-on-Si samples for ellipsometry measurements (see Supporting Information Part 1). In our calculations, we assume that the ITO carrier concentration is $N_0 = 2.8 \times 10^{20}$ cm^{-3}. Our electrostatics calculations show that the work function of ITO with carrier concentration $N_0 = 2.8 \times 10^{20}$ is 4.4 eV, which is lower than the work function of gold (W_f^{Au} = 5.1 eV). This results in electron depletion at the Al_2O_3/ITO interface and band bending in the ITO for applied voltage $V = 0$. When the electrical bias applied between the antenna and ITO is larger than 1 V, an electron accumulation layer is formed in ITO at the Al_2O_3/ITO interface (for a detailed discussion, see Supporting Information Part 2). Figure 1b (bottom) shows the calculated ε_r^{ITO} for different applied biases as a function of distance from the Al_2O_3/ITO interface at an operation wavelength of 1550 nm. The dielectric permittivity of ITO substantially changes over the region within around 2 nm of the Al_2O_3/ITO interface due to the formation of the accumulation layer. The gray area highlights the ENZ region of ITO where ε_r^{ITO} acquires values between 1 and −1. Under a positive bias, the value of ε_r^{ITO} at the Al_2O_3/ITO interface decreases, reaching the ENZ condition at an applied bias of 2.9 V. Furthermore, the thickness of the ENZ region can be estimated as 0.9 nm at an applied bias of 5 V. Importantly, when the ENZ condition holds, a large electric field enhancement is generated in the accumulation layer of ITO. This can be readily understood from the boundary condition, imposing continuity of the

DOI: 10.1021/acs.nanolett.6b00555
Nano Lett. 2016, 16, 5319−5325

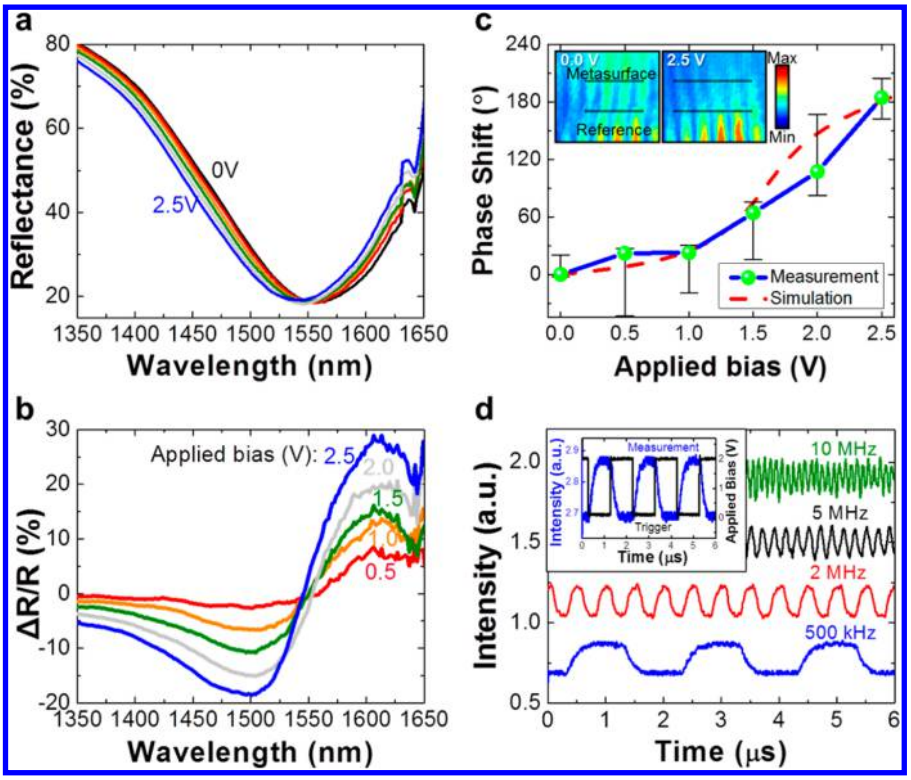

Figure 3. Experimental demonstration of π-phase modulation and amplitude modulation in tunable metasurfaces. (a) Measured reflectance spectrum and (b) relative reflectance change from the metasurface for different applied voltages. Relative reflectance change is defined as the ratio of reflectance change due to applying bias $[\Delta R = R(V) - R(0)]$ and the reflectance without applied bias $[R(0)]$. (c) Measured and simulated phase shift as a function of applied bias for applied voltage between 0 and 2.5 V. Inset: the interference fringes for applied bias 0 and 2.5 V. The black lines show the cross-section for analyzing the phase. (d) Measured high speed reflectance modulation with modulation frequencies from 500 kHz to 10 MHz. Inset: Measured ac modulated reflectance with operation speed of 500 kHz.

normal component of the electric displacement at the field effect dielectric/channel interface.[26,33,34]

A photographic image of the final device, fabricated by multilayer deposition and e-beam lithography is shown in Figure 1c. One can visually distinguish the Au back plane, ITO, electrical connections, and electrodes (for further fabrication details, see Supporting Information Part 3). Scanning electron microscope images of a stripe antenna structure are depicted in Figure 1d,e. Adjacent stripe antennas are connected electrically in groups of three so that each group is connected to a different external gold electrode. The electrodes are wire connected to a compact chip carrier and circuit board for electrical gating.

Electromagnetic Simulations of Tunable Metasurfaces. Using finite element electromagnetic simulation methods, we simulated reflectance and phase modulation of the periodically patterned antenna structure under normal incidence illumination with a transverse magnetic (TM) polarization (H-field along the stripes). We consider an array of w = 250 nm wide and t_1 = 50 nm thick Au stripe antennas arranged with periodicity of p = 400 nm. The stripe antenna array is on top of a 5 nm thick Al_2O_3 layer on a 20 nm thick ITO layer and 80 nm thick Au back plane (Figure 1a). Figure 2a,b shows the reflectance and phase shift spectra as a function of applied voltage. Phase shift spectra are calculated by simply taking the difference between the phase of the reflected field with and without bias. The dotted lines indicate the ENZ region in the accumulation layer of ITO at the Al_2O_3/ITO interface, and the green dashed line marks the position of a reflectance dip corresponding to the magnetic dipole plasmon resonance. With increasing gate bias, the magnetic dipole plasmon resonance couples to the ENZ region in the ITO accumulation layer that shifts the resonance and induces a significant phase shift in reflection.

As one can see, there are two different regimes describing coupling of the antenna plasmonic resonance with the ENZ region in ITO. For an increasing bias from 0 to around 3 V, the antenna plasmonic resonance shifts to shorter wavelengths due to an increase in the carrier concentration and reduction of ε_r^{ITO}. As the resonance blue shifts (at applied biases from 0 to 3 V), the phase shift at 1550 nm dramatically increases. As one can see from Figure 2c, the calculated phase shift as a function of applied bias at 1550 nm shows close to 180° phase shift at 3.0 V and 225° phase shift at 4.6 V. In the case of an applied bias around 3 V, ε_r^{ITO} becomes zero. Applying a higher voltage (>3 V), the plasmonic resonance shifts to longer wavelengths. This change in the sign of the resonant wavelength shift can be intuitively understood by looking at the behavior of the optical properties of the ITO layer. With an increased bias larger than 3 V, the carrier concentration in the ITO at Al_2O_3/ITO interface increases, and this accumulation layer functions optically as a metal ($\varepsilon_r^{ITO} < 0$), thus shrinking the effective thickness of the dielectric spacer (Al_2O_3 and ITO layers) and shifting the magnetic resonance to longer wavelengths.[35]

Our simulations show that even though the ITO permittivity is only modulated within a 2 nm thick layer at the interface, this change introduces a shift in the resonance wavelength of around 19 nm and phase shift of 225° at applied bias of 4.6 V (Figure 2c). To gain further insight, the distribution of electromagnetic field at different applied voltages is shown in Figure 2d,e. At 0 V, ITO optically behaves as a dielectric (ε_r^{ITO}

DOI: 10.1021/acs.nanolett.6b00555
Nano Lett. 2016, 16, 5319−5325

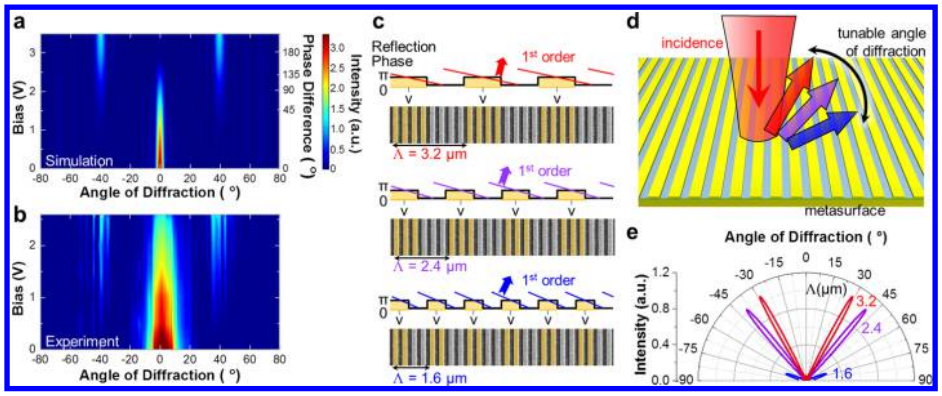

Figure 4. Dynamic phase grating with wide angular tunability. (a) Simulated far-field intensity profiles of the diffracted beam versus applied bias. The color map shows far-field intensity of the light beam reflected from the metasurface as a function of diffraction angles and applied voltages (and corresponding phase difference via electrical gating of different voltage on the antennas) for normal incidence. (b) Experimental measured far-field intensity profiles (detection angle up to ~50° with 0.75 NA objective lens). (c,d) Schematic of steering diffracted beam angles via electrical gating of different number of antennas showing wide angular beam steering with high resolution. Periodically gating of 4, 3, 2 antennas effectively generate grating periodicities of 3.2, 2.4, 1.6 μm, respectively. (e) Simulated far-field intensity of the light beam reflected from the metasurface as a function of the diffraction angles for periodicities of 3.2, 2.4, 1.6 μm under a gate bias of 3.0 V. The device demonstrates an efficient beam steering with large range of angles (>40°) with 2−4 periodically gated nanoantennas.

> 0), and at the resonance we observe antiparallel electric fields characteristic of a magnetic dipole between the Au antenna and Au back plane (see Supporting Information Part 4 for further field analysis). For applied bias values larger than 1.8 V, when the ENZ condition holds in the accumulation layer of the ITO, the enhancement of the z-component of the electric field (E_z) in the accumulation layer is observed (see second and third image in Figure 2e) due to continuity of the normal component of electric displacement ($\varepsilon_\perp E_\perp$) at the interface of the two media. In the case of applied voltage of 3.0 V, where $\varepsilon_r^{ITO} \sim 0$ in the accumulation layer, E_z is enhanced in a direction parallel to the field in the Al_2O_3 and bulk ITO (second image in Figure 2e). In contrast, for applied voltage of 4.6 V (third image in Figure 2e), because the permittivity of ITO in some region of the accumulation layer is negative (metal-like), the E_z component is antiparallel to the field in the Al_2O_3 and bulk ITO layers. The enhanced parallel and antiparallel E_z due to coupling to ENZ region further modifies the strength of the magnetic dipole and the phase shift profile as can be seen in Figure 2e, resulting in a large phase modulation via electrical gating.

Experimental Results. The reflectance spectrum and phase shift are measured for different applied biases as shown in Figure 3 (see Supporting Information Part 5 for reflectance measurement setup). In Figure 3a, we experimentally observe that the experimental resonance shifts to shorter wavelengths by around 17 nm when increasing voltage from 0 to 2.5 V. The wavelength and reflectance values at the resonance dip minimum match well with the simulation results (c.f., Figures 3a and 2a), as does the wavelength shift with applied bias. The reflectance change (normalized to the reflectance without applied voltage, $\Delta R/R = [R(V) - R(0)]/R(0)$) is as high as 28.9% for operating wavelengths near the resonant reflectance minimum under an applied bias of 2.5 V (Figure 3b), indicating gate-actuated metasurface reflectance amplitude modulation. To measure the phase shift, a Michelson interferometer was used to observe interference fringes where the incident beam is positioned at the edge of the metasurface so that part of the beam is reflected from the metasurface and part is reflected from the planar multilayer stack of Al_2O_3/ITO/Au-back-plane, which acts as a built-in phase self-reference. Note that this self-referenced phase interferometry configuration allows accurate phase measurement, eliminating errors caused by vibration or instability, because the reference and measured phases are captured at the same time and location (see Supporting Information Part 6 for phase measurement setup). The phase shift measurements were performed at a wavelength of λ = 1573 nm. Typical interference fringe images formed by the light reflected from the sample at zero applied bias and at an applied bias of 2.5 V are shown in the inset of Figure 3c. The fringes from the patterned area of the sample shift to the left by about half a period as compared to the reference fringes. Phase shifts were retrieved at different applied voltages by fitting and analyzing the amplitudes (shown in black line in the inset of Figure 3c) of interference fringes (see Supporting Information Part 6 for a detailed phase analysis). The results are shown in Figure 3c. It is clear that the phase shift (green circles with blue line as a guide to the eye) increases with applied bias. A phase change of ~184° is observed at applied bias of 2.5 V, which is in a good agreement with simulation results (red dashed line). The error bars on the green circles indicate the phase shift error that is in reasonable accord with simulations (see Supporting Information Part 6 for a detailed analysis of experimental errors). Note that the obtained phase shift matches well with the simulation results (see Supporting Information Part 1 for assumed parameters of ITO). It should be noted that the working wavelength changes slightly from 1550 (Figure 2c) to 1573 nm (Figure 3c) because of the small structural nonuniformity between the center and the edge of the sample (width of the stripe changes from 252 to 258 nm, see Supporting Information Part 7 for details). We also applied negative bias voltages that further deplete the ITO at the Al_2O_3/ITO interface, in contrast to the positive bias voltages. In the case of a negative applied bias, a red shift of the resonant reflectance minimum is observed, indicating that we can both increase and decrease ε_r^{ITO} near the Al_2O_3/ITO interface by applying positive or negative biases, respectively. This excludes alternative interpretations of the observed resonance shift mechanisms including but not limited to thermal (Joule) heating (Supporting Information Part 8). We note that the 5 nm Al_2O_3 layer exhibits electrical breakdown at around 2.5−3 V.

DOI: 10.1021/acs.nanolett.6b00555
Nano Lett. 2016, 16, 5319−5325

To characterize the frequency response of our tunable metasurfaces, a 2 V bias with frequencies ranging from 0.5−10 MHz was applied to the sample and a high speed InGaAs detector was used to detect the temporal metasurface reflectance. To ensure high enough ratio of reflected light intensity during on and off cycles of the measurement, that is, high $\Delta R/R$, we selected an off-resonant wavelength to perform modulation bandwidth measurements (Supporting Information Part 9). As shown in the inset of Figure 3d, high speed reflectance modulation is observed by applying 2 V of 500 kHz ac signal (blue curve). In addition, modulation speeds as high as 10 MHz were demonstrated (see Figure 3d). Note that the waveform is distorted at the highest frequencies due to the detector bandwidth. The metasurface at 2 MHz frequency for different applied biases was also investigated and a ∼15% of reflectance amplitude modulation is obtained with a 2 V applied voltage (Supporting Information Part 10).

The maximum speed of the modulation can be estimated using a simple device physics calculation, which gives a capacitance value of 14 fF/μm^2 per unit area (Supporting Information Part 10). For our antenna array, this would yield capacitance and resistance values of 140 fF and 100 Ω per wire (area = 50 μm × 0.2 μm), respectively. Such a small capacitance could thus in principle enable modulation speeds up to 11 GHz and switching energies as low as 0.7 pJ/bit (this estimate does not include other sources of signal delay resulting from the wiring and RF probe connections). Note that the individual antenna can be implemented in a two-dimensional antenna array with a smaller footprint (0.2 μm × 0.2 μm) and capacitance (0.5 fF). With 100 Ω resistance per pixel, this would enable 2.5 fJ switching energies per bit and up to 3 THz modulation speeds (although the speed could be limited by interconnect with current speed values up to ∼100 GHz).[36]

Demonstration of a Dynamic Phase Grating. As demonstrated in both experimental and simulated results, a large phase change (∼184°) can be achieved. We further employ the tunable phase shift to develop an electrically driven dynamic phase grating. The voltage-dependent far-field intensity profiles of a metasurface phase grating with 48 unit cells consisting of identical stripe antennas on Al_2O_3/ITO/Au planar layers were simulated. Figure 4a shows the far field diffracted beam profile of a 2-level phase grating with a periodicity of Λ = 2.4 μm operating at wavelength 1550 nm. At applied bias of 0 V, the diffracted beam shows a directional reflectance (zeroth order diffraction beam only) from the sample. At the applied bias of 3.0 V, the 2-level phase grating creates two symmetric first-order diffracted beams with maximum intensity at angles of approximately −40 and 40° due to the spatial symmetry of the structure, while the zeroth order diffraction beam almost disappears. The experimentally measured far-field diffracted beam intensity operating at wavelength 1550 nm is depicted in Figure 4b. It can be seen that the ±first order diffracted beams appear with applied voltage ∼>1.5 V while the zero-order diffracted beam intensity reduces with increasing voltage, in agreement with the simulation results (Figure 4a). These results demonstrate electrical tunability of reflection phase at a stripe antenna level, which forms a fundamental basis for tunable optical phased array metasurfaces. Note that the slight discrepancy on the diffracted angles and beam widths between the simulated and measured results can be attributed to the nonparallel incident light excitation from the high NA objective and the slight nonuniformity of the sample. Importantly, the diffracted beam angle can also be varied by gating multiple antennas with different periodicities Λ for steering diffracted beam angles (Figure 4c−e). As shown in Figure 4c, gating of 4, 3, and 2 antennas periodically will yield grating periods of 3.2, 2.4, and 1.6 μm, respectively (the distance between centers of neighboring antennas is 400 nm), leading to ability to control diffracted beam angles (see schematics in Figure 4c,d). To demonstrate the tunability of the first order diffraction angle, we simulate the far-field intensity of the first order diffracted beam for different grating periods at applied bias of 3.0 V (Figure 4e). The diffracted beam can be effectively steered over a wide range of angles (>40°) by gating subgroups of 4, 3, 2 antennas. Hence, the designed structure functions as a nanoscale beam steering device. To obtain a narrower beam width, we can increase total number of antenna unit cells. One could in principle, via separate electrical connection to each antenna, further modify the phase grating to achieve continuous steering of the diffracted beam or to synthesize dynamic holographic images.[6] These efficient wide-angle electronically tunable beam steering components have considerable potential for the development of next generation ultrathin on-chip imaging and sensing devices, such as high resolution LIDARs (a portmanteau of "light" and "radar") and nanoscale spatial light modulators.

In summary, we report an experimental and simulated demonstration of a tunable metasurface in the near-infrared wavelength region. We control the phase and amplitude of the reflected light by gate-tunable field effect dynamical permittivity modulation. A phase shift of 184° and reflectance change of ∼30% were measured by applying 2.5 V gate bias. A modulation speed of up to 10 MHz (with potential modulation speed up to 11 GHz) and electrical beam-steering of ±first order diffracted beams were also demonstrated. In addition to the fundamental interest of tunable metasurfaces, these structures have many potential applications for future ultrathin optical components, such as dynamic holograms, tunable ultrathin lens, reconfigurable beam steering devices, nanoprojectors, and nanoscale spatial light modulators.

■ ASSOCIATED CONTENT

Ⓢ Supporting Information

The Supporting Information is available free of charge on the ACS Publications website at DOI: 10.1021/acs.nanolett.6b00555.

Experimental and simulation details on the optical properties of ITO, fabrication of metasurfaces, field analysis, reflection and phase measurement setups, phase analysis, structural nonuniformity, reflectance measurements with negative biases, high frequency ac modulation, and IV measurements (PDF)

■ AUTHOR INFORMATION

Corresponding Author

*E-mail: haa@caltech.edu.

Present Address

(H.W.H.L.) Department of Physics, Baylor University, Waco, Texas 76798, United States; The Institute for Quantum Science and Engineering, Texas A&M University, College Station, TX 77843, United States.

Author Contributions

(Y.W.H. and H.W.H.L.) contributed equally to this work. Y.W.H., H.W.H.L., R.S., and H.A.A. designed and conceived the

DOI: 10.1021/acs.nanolett.6b00555
Nano Lett. 2016, 16, 5319−5325

experiments. Y.W.H. and H.W.H.L. fabricated the samples. Y.W.H., H.W.H.L., and R.A.P developed the measurement setup and performed the experiments. Y.W.H., H.W.H.L., and K.T. performed materials characterizations. Y.W.H. and R.S. performed numerical simulations. Y.W.H., H.W.H.L., R.S., R.A.P., K.T., S.H., and H.A.A. wrote the paper. All authors discussed the results and commented on the manuscript.

Notes

The authors declare no competing financial interest.

■ ACKNOWLEDGMENTS

This work was supported by Samsung Electronics and by the Hybrid Nanophotonics Multidisciplinary University Research Initiative Grant (Air Force Office of Scientific Research, FA9550-12-1-0024). The conducting oxide material synthesis design and characterization was supported by the U.S. Department of Energy (DOE) Office of Science grant DE-FG02-07ER46405 (K.T. and H.A.A.) and used facilities supported by the Kavli Nanoscience Institute (KNI) and Joint Center for Artificial Photosynthesis (JCAP) at Caltech. Y.W.H. and D.P.T. acknowledge the support from Ministry of Science and Technology, Taiwan (Grants 103-2911-I-002-594, 104-2745-M-002-003-ASP, and 105-2745-M-002-002-ASP) and Academia Sinica (Grant AS-103-TP-A06). K.T. acknowledges funding from the Swiss National Science Foundation (Grant 151853). The authors would like to thank Rui Liu for Al_2O_3 deposition and Katherine Fountaine for useful discussions.

■ REFERENCES

(1) Yu, N.; Genevet, P.; Kats, M. A.; Aieta, F.; Tetienne, J.-P.; Capasso, F.; Gaburro, Z. *Science* **2011**, *334*, 333−337.
(2) Yu, N.; Capasso, F. *Nat. Mater.* **2014**, *13*, 139−150.
(3) Kildishev, A.; Boltasseva, A.; Shalaev, V. *Science* **2013**, *339*, 1232009.
(4) Chen, W. T.; Yang, K.-Y.; Wang, C.-M.; Huang, Y.-W.; Sun, G.; Chiang, I.-D.; Liao, C. Y.; Hsu, W.-L.; Lin, H. T.; Sun, S.; et al. *Nano Lett.* **2014**, *14*, 225−230.
(5) Zheng, G.; Muhlenbernd, H.; Kenney, M.; Li, G.; Zentgraf, T.; Zhang, S. *Nat. Nanotechnol.* **2015**, *10*, 308−312.
(6) Huang, Y.-W.; Chen, W. T.; Tsai, W.-Y.; Wu, P. C.; Wang, C.-M.; Sun, G.; Tsai, D. P. *Nano Lett.* **2015**, *15*, 3122−3127.
(7) Ni, X. J.; Kildishev, A. V.; Shalaev, V. M. *Nat. Commun.* **2013**, *4*, 2807.
(8) Yin, X. B.; Ye, Z. L.; Rho, J.; Wang, Y.; Zhang, X. *Science* **2013**, *339*, 1405−1407.
(9) Genevet, P.; Yu, N. F.; Aieta, F.; Lin, J.; Kats, M. A.; Blanchard, R.; Scully, M. O.; Gaburro, Z.; Capasso, F. *Appl. Phys. Lett.* **2012**, *100*, 013101.
(10) Lin, D.; Fan, P.; Hasman, E.; Brongersma, M. *Science* **2014**, *345*, 298−302.
(11) Meinzer, N.; Barnes, W.; Hooper, I. *Nat. Photonics* **2014**, *8*, 889−898.
(12) Yu, N. F.; Aieta, F.; Genevet, P.; Kats, M. A.; Gaburro, Z.; Capasso, F. *Nano Lett.* **2012**, *12*, 6328−6333.
(13) Sautter, J.; Staude, I.; Decker, M.; Rusak, E.; Neshev, D. N.; Brener, I.; Kivshar, Y. S. *ACS Nano* **2015**, *9*, 4308−4315.
(14) Buchnev, O.; Podoliak, N.; Kaczmarek, M.; Zheludev, N.; Fedotov, V. *Adv. Opt. Mater.* **2015**, *3*, 674−679.
(15) Lee, J.; Jung, S.; Chen, P.; Lu, F.; Demmerle, F.; Boehm, G.; Amann, M.; Alu, A.; Belkin, M. *Adv. Opt. Mater.* **2014**, *2*, 1057−1063.
(16) Yao, Y.; Shankar, R.; Kats, M.; Song, Y.; Kong, J.; Loncar, M.; Capasso, F. *Nano Lett.* **2014**, *14*, 6526−6532.
(17) Decker, M.; Kremers, C.; Minovich, A.; Staude, I.; Miroshnichenko, A.; Chigrin, D.; Neshev, D.; Jagadish, C.; Kivshar, Y. *Opt. Express* **2013**, *21*, 8879−8885.
(18) Waters, R. F.; Hobson, P. A.; MacDonald, K. F.; Zheludev, N. I. *Appl. Phys. Lett.* **2015**, *107*, 081102.
(19) Goldflam, M. D.; Liu, M. K.; Chapler, B. C.; Stinson, H. T.; Sternbach, A. J.; McLeod, A. S.; Zhang, J. D.; Geng, K.; Royal, M.; Kim, B. J.; et al. *Appl. Phys. Lett.* **2014**, *105*, 041117.
(20) Dabidian, N.; Kholmanov, I.; Khanikaev, A. B.; Tatar, K.; Trendafilov, S.; Mousavi, S. H.; Magnuson, C.; Ruoff, R. S.; Shvets, G. *ACS Photonics* **2015**, *2*, 216−227.
(21) Park, J.; Kang, J. H.; Liu, X.; Brongersma, M. L. *Sci. Rep.* **2015**, *5*, 15754.
(22) Olivieri, A.; Chen, C.; Hassan, S.; Lisicka-Skrzek, E.; Tait, R. N.; Berini, P. *Nano Lett.* **2015**, *15*, 2304−2311.
(23) Jun, Y. C.; Reno, J.; Ribaudo, T.; Shaner, E.; Greffet, J. J.; Vassant, S.; Marquier, F.; Sinclair, M.; Brener, I. *Nano Lett.* **2013**, *13*, 5391−5396.
(24) Feigenbaum, E.; Diest, K.; Atwater, H. A. *Nano Lett.* **2010**, *10*, 2111−2116.
(25) Dionne, J. A.; Diest, K.; Sweatlock, L. A.; Atwater, H. A. *Nano Lett.* **2009**, *9*, 897−902.
(26) Lee, H. W.; Papadakis, G.; Burgos, S. P.; Chander, K.; Kriesch, A.; Pala, R.; Peschel, U.; Atwater, H. A. *Nano Lett.* **2014**, *14*, 6463−6468.
(27) Naik, G. V.; Kim, J.; Boltasseva, A. *Opt. Mater. Express* **2011**, *1*, 1090−1099.
(28) Boltasseva, A.; Atwater, H. A. *Science* **2011**, *331*, 290−291.
(29) Melikyan, A.; Lindenmann, N.; Walheim, S.; Leufke, P. M.; Ulrich, S.; Ye, J.; Vincze, P.; Hahn, H.; Schimmel, T.; Koos, C.; et al. *Opt. Express* **2011**, *19*, 8855−8869.
(30) Sorger, V. J.; Lanzillotti-Kimura, N. D.; Ma, R. M.; Zhang, X. *Nanophotonics* **2012**, *1*, 17−22.
(31) Yi, F.; Shim, E.; Zhu, A. Y.; Zhu, H.; Reed, J. C.; Cubukcu, E. *Appl. Phys. Lett.* **2013**, *102*, 221102.
(32) Shi, K. F.; Haque, R. R.; Zhao, B. Y.; Zhao, R. C.; Lu, Z. L. *Opt. Lett.* **2014**, *39*, 4978−4981.
(33) Lu, Z.; Zhao, W.; Shi, K. *IEEE Photonics J.* **2012**, *4*, 735−740.
(34) Vasudev, A. P.; Kang, J. H.; Park, J.; Liu, X. G.; Brongersma, M. L. *Opt. Express* **2013**, *21*, 26387−26397.
(35) Dolling, G.; Enkrich, C.; Wegener, M.; Zhou, J. F.; Soukoulis, C. M. *Opt. Lett.* **2005**, *30*, 3198−3200.
(36) Chen, G.; Chen, H.; Haurylau, M.; Nelson, N. A.; Albonesi, D. H.; Fauchet, P. M.; Friedman, E. G. *Integration, VLSI J.* **2007**, *40*, 434−446.

DOI: 10.1021/acs.nanolett.6b00555
Nano Lett. 2016, 16, 5319−5325